RESEARCH ARTICLE

Supercapacitor

Energy & Environmental Materials WILEY

Coaxial Core–Shell Carbon–Tin Sulfide Nanohybrids as High-Performance Electrodes for Long-Life Supercapacitors

*Anjana Baby, Janez Zavasnik, Janez Kovač, and Neelakandan M. Santhosh**

As emerging high-power energy devices, supercapacitors require electrode materials that enable fast charge transport at high current and long-term stability. In this regard, integrating electric double-layer capacitance with pseudocapacitive behavior in metal sulfide–carbon nanohybrids is a promising strategy to enhance both capacitance and cycling stability. Herein, a coaxial core–shell carbon–tin sulfide nanohybrid is designed as a high-performance binder-free electrode using a rapid plasma-assisted dry approach, enabling uniform overgrowth of layered SnS on vertical nanocarbon (VCN) to form SnS@VCN. The strong interface interaction and conductive carbon framework synergistically enhance ion transport and structural stability, resulting in one of the best SnS-based electrode performances by delivering a high specific capacitance of 577 F g^{-1} (242 C g^{-1}) at 3 A g^{-1} and retaining 72% of its capacitance at 12 A g^{-1} with a remarkable cyclic stability of 115% capacitance retention after 10 000 cycles. An asymmetric SnS@VCN//AC device further delivers a specific capacitance of 17.8 F g^{-1} and ultrahigh cyclic stability, with 140% capacitance retention after 5000 cycles. The interplay between the plasma-tailored interface and hierarchical core–shell morphology effectively overcomes the rate and stability limitations of conventional battery-type electrodes, offering a scalable, environmentally benign pathway toward ultra-stable, high-rate energy storage materials for advanced supercapacitors.

1. Introduction

Growing global demand, along with rapid technological advancements in miniaturized devices and portable electronics, has highlighted the importance of sustainable energy storage solutions to meet consumer needs. Addressing these challenges depends on efficient energy storage systems, where electrochemical technologies are considered a key factor. Among various electrochemical energy-storage devices, supercapacitors (SCs) are currently gaining significant attention from both academia and industry due to their standout features, including fast charge–discharge rates, high-power density, and exceptional cycling stability.[1,2] Despite these benefits, the large-scale application of supercapacitors is often hindered by their relatively low-energy density compared with conventional batteries.[3] Addressing this limitation remains a critical challenge; fabricating high-performance supercapacitors with enhanced energy density and prolonged cycle life is critical to meet the increasing energy requirements across diverse applications. The performance of SCs primarily depends on the energy-storage capabilities of electrode materials; thus, the rational design and synthesis of electrode materials with tailored electrochemical characteristics have become a key focus in the field.

Materials with redox-based charge-storage characteristics are expected to deliver high energy-storage performance owing to their high electrical conductivity, which enables rapid charge-carrier transport from the electrolyte to the electrode interface; excellent electrochemical stability, which prevents unwanted reactions with the electrolyte; and their high surface area, as capacity scales with the interfacial area.[4–8] In this regard, metal chalcogenides with pseudocapacitive behavior have attracted significant interest for supercapacitors due to their ability to undergo faradaic redox reactions within the material upon voltage application.[9,10] Owing to lower electronegativity, sulfur-based materials enable more efficient electron transfer, improve charge-transport kinetics, and yield a strong potential for metal sulfide-based electrodes for SCs. Among various metal sulfides, tin sulfide (SnS) has attracted considerable attention owing to its layered crystal structure, high theoretical capacitance, robust chemical stability, and inherent electrical conductivity.[11,12] The presence of multiple oxidation states in Sn activates faradaic reactions, while sulfide anions (S^{2-}) improve electrical conductivity, provide additional redox sites, and enable efficient ion transport through the layered framework.[13] Several studies have demonstrated the potential of SnS-based electrodes in high-performing SC applications. A few examples using SnS-based electrodes, including nanoflakes synthesized via colloidal methods, exhibited a remarkable capacitance of 582 F g^{-1} at 8 A g^{-1},[14] and SnS nanorods showed promising energy and power densities of 1.49 Wh kg^{-1} and 248.33 W kg^{-1}, respectively, highlighting the future opportunities of the material.[15] Despite these advantages, SnS still suffers from relatively low electrical conductivity and

Dr. A. Baby, Prof. J. Zavasnik, Prof. N. M. Santhosh
Department of Gaseous Electronics (F6), Jožef Stefan Institute, Jamova cesta 39, Ljubljana SI-1000, Slovenia
E-mail: neelakandan.marath.santhosh@ijs.si
Prof. J. Zavasnik
Max-Planck-Institut für Nachhaltige Materialien, Max-Planck-Straße 1, 40074, Düsseldorf, Germany
Prof. J. Kovač
Department of Surface Engineering (F4), Jožef Stefan Institute, 1000, Ljubljana, Slovenia
The ORCID identification number(s) for the author(s) of this article can be found under https://doi.org/10.1002/eem2.70429.

DOI: 10.1002/eem2.70429

moderate cycling stability, which limit efficient charge transport.[16,17] Incorporating or hybridizing with highly conductive carbon nanostructures can effectively overcome these challenges by providing enhanced electrical pathways, structural stability, and additional electroactive sites, thereby improving supercapacitor performance. Growth/deposition of active materials directly on the current collector is considered a feasible approach for providing free-standing hierarchical electrodes with a large electrode–electrolyte contact area to improve electrochemical reactions.[18] Such hierarchical structures can neglect the need for polymeric binders used in electrode preparation, thereby minimizing resistivity-related issues during electrochemical testing.

Thus, designing an advanced electrode material based on a SnS hybrid with carbon nanostructures directly on a substrate could overcome the issues related to poor conductivity and the side effects of binders, thereby improving energy storage performance. The direct growth of hierarchical carbon nanomaterials on various substrates using chemical vapor deposition, arc-discharge method, electrochemical synthesis, and plasma-enhanced chemical vapor deposition (PECVD) has been widely reported.[19–21] Among these techniques, PECVD stands out for its ability to achieve the fastest, most controllable growth of nanostructures with diverse morphologies and orientations.[20,22] Depending on the plasma discharge conditions, nanocarbons can form nanotubes, nanowalls, or nanospheres with either vertical or horizontal dimensions.[23–25] The plasma-assisted method offers significant advantages over conventional wet synthesis by eliminating the need for solvents, enabling rapid processing, and allowing precise control over surface morphology and defect formation.[26] Such plasma-designed nanocarbon, with excellent adhesion to the substrate surface, can serve as a backbone for anchoring various metal sulfides, which can be used as efficient electrodes for SCs.[4,27] Such hybrid nanocarbon–metal sulfide electrodes exhibit unique electrochemical properties compared with metal sulfides and carbon when used individually as active materials. As a result, the composite provides a higher capacity, better cycling stability, and good rate capability, making it suitable for assembling high-capacity redox-based SCs. In addition, such a combination of electrodes could help mitigate the limitations of redox supercapacitors, which suffer from poor stability and rate capability.

Therefore, this work explores improving the electrochemical performance of SnS by integrating it with vertical nanocarbons (VCNs). The unique hierarchical and anisotropic structure of the VCN arrays amplifies the inherent mechanical, electrical, and thermal properties of individual nanotubes, extending these advantages to the bulk material scale. Unlike conventional synthesis methods, which are time-consuming and rely on chemical reagents, this work demonstrates a plasma-enabled, soft-chemistry, dry approach to grow SnS@VCN nanohybrids directly and evaluates their potential to enhance charge storage in SC applications. Comprehensive structural and morphological analyses revealed that the SnS anchored on highly conductive VCN exhibits high structural quality and electrochemical stability, enabling long-term device performance without degradation. The plasma-designed binder-free SnS@VCN electrodes exhibited a faradaic "battery-like" electrochemical response and delivered one of the highest discharge capacities (577 F g^{-1} @ 3 A g^{-1}) among SnS-based electrodes. To date, one of the main challenges in translating these faradaic materials into SC electrodes has been poor rate capability and long-term stability, which were significantly addressed in this work by maintaining 72% of the initial capacitance at a higher current density of 12 A g^{-1} and retaining an increased (>100%) capacitance after 10 000 cycles. Similarly, an asymmetric capacitor fabricated with SnS@VCN as the active material exhibited comparable energy and power densities, along with ultrahigh stability, maintaining increased capacitance after 5000 cycles. The unique conformal core–shell nanotubular heterostructure of SnS@VCN, with controlled structural defects and a hierarchical morphology, exhibits minimum contact resistance and enhances electrochemical performance and charge storage. By combining rapid processing, mild conditions, and environmental compatibility, this plasma-enabled strategy for engineering high-performance electrodes offers a viable pathway toward advancing next-generation supercapacitor systems.

2. Results and Discussions

2.1. Morphological Characterization

The initial nanocarbon deposition on the nickel foam substrate was followed a catalyst-assisted PECVD process, as reported elsewhere, yielding vertically aligned individual nanotube arrays, VCNs. The VCN structures are homogeneously distributed on the substrate surface. The as-grown VCNs form closely packed tube-like structures, as shown in **Figure 1**a. The VCN structures possess an average height of 1–2 μm and a diameter of ∼100 nm and are terminated by a single-crystal Ni particle (Figure 1b). Changes in the surface morphology of VCN after the plasma deposition of the Sn layer, followed by the plasma sulfurization to SnS, are presented in Figure 1d,e. The observed morphological difference is the expansion of the diameter of the individual hybrid nanostructure to ∼200 nm, while the length and orientation of the VCNs remain the same as before deposition. The SnS is fully anchored to the VCN backbone in a coaxial core–shell morphology, thereby simultaneously ensuring electrical conductivity and pseudocapacitive behavior. Additionally, each SnS@VCN nanostructure is separated by a void, which could help mitigate volume change during repeated ion insertion/extraction during electrochemical reactions, enabling long-term stability under harsh electrolyte conditions. The presence of Sn and S after the plasma conversion on the VCN backbone is confirmed by EDS analysis presented in Figure S1, Supporting Information.

Further insights into the structure and morphology of the VCN and SnS@VCN hybrid structure were obtained by TEM. The overview micrographs show that the VCN is a multiwalled carbon structure with a diameter of ∼100 nm and a single-crystal Ni nanoparticle at its tip (Figure 1c), similar to the previously reported tip-growth mechanism in plasma-grown VCN structures.[28,29] The TEM micrograph of the SnS deposited VCN structures confirms the overall morphology as observed from SEM, and that the VCN backbone is fully overgrown by SnS (**Figure 2**a) with a thickness of the SnS deposit of ∼100 nm (Figure 2b). The surface details reveal a layered structure, clearly visible due to edge folding (Figure 2c). The individual sheets are 5–10 nm thick and measure up to 50 nm in diameter, with the individual layers separated by ∼5.85–5.87 Å, as measured directly from FFT patterns (Figure 2 FFT). The sheets are often bent, twisted, and folded, and contain multiple defects. The phase composition of the Sn-S phase was analyzed by SAED; the experimental pattern coincides with the reference data for orthorhombic SnS (S.G.: Pnma), and no other phases were detected (Figure 2d,e). The chemical composition was assessed by STEM-EDS analysis; the EDS spectra are shown in Figure 2f, along with the STEM micrograph with a marked point EDS analysis spot. The EDS mapping confirms the homogeneous distribution of Sn and S throughout the carbon backbone (Figure 2g), indicating that the SnS@VCN

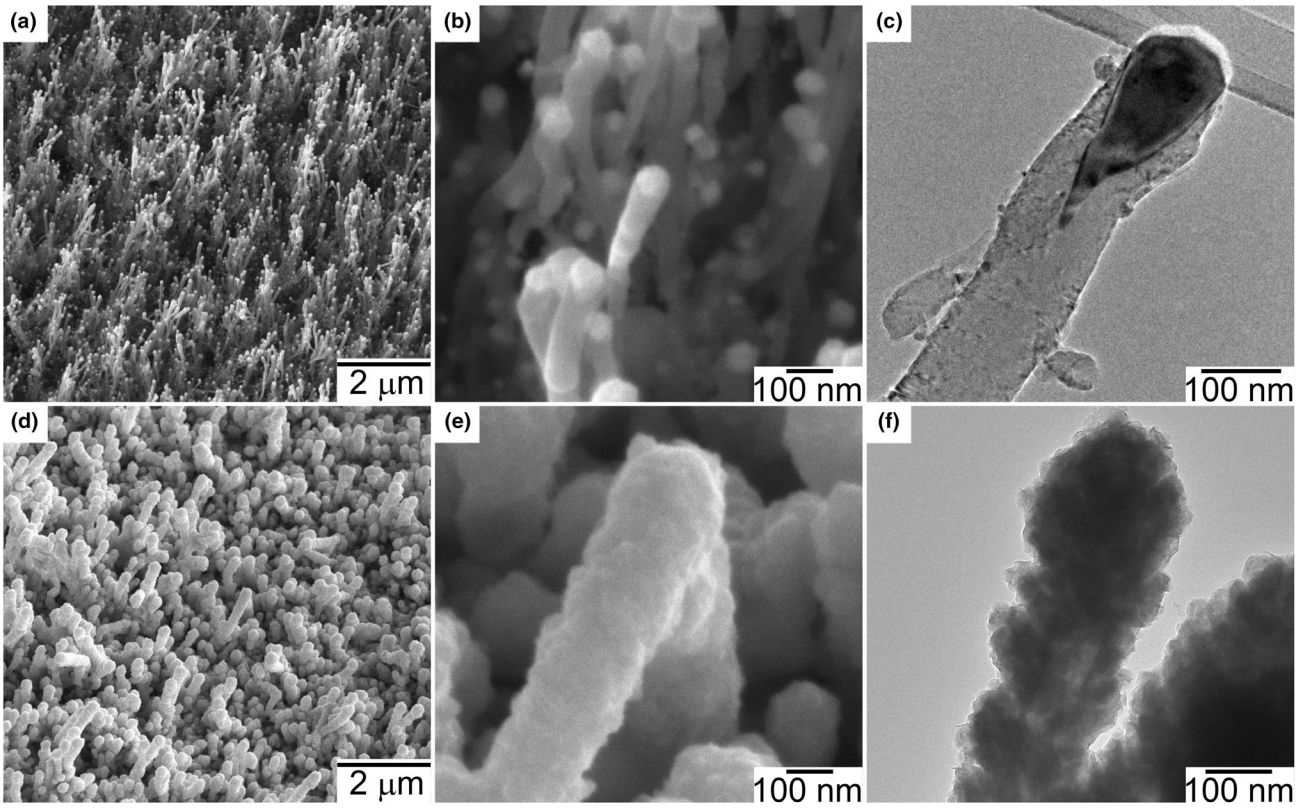

Figure 1. Surface morphology of plasma-designed VCN and SnS@VCN nanostructures. a, b) Tilted view SEM-SE micrographs of homogeneously grown VCN; d, e) tilted view SEM-SE micrographs of SnS@VCN after plasma sulfurization process; c, f) overview conventional TEM micrographs of plasma-designed VCN and SnS@VCN.

nanostructure obtained exhibits a hybrid, coaxial, core–shell-like morphology.

To understand the structural organization of the designed coaxial core–shell structured SnS@VCN hybrids, the nanostructures were further evaluated by Raman spectroscopy, and the resulting spectra are presented in **Figure 3**a. Both VCN and SnS@VCN featured characteristic graphitic behavior with peaks around 1358 cm^{-1} (D band), 1572 cm^{-1} (G band), 2697 cm^{-1} (2D band), and 2938 cm^{-1} (D + G band).[4,28] The presence of well-defined D, G, and 2D peaks indicates a highly ordered graphitic nature, along with some structural defects in both structures, which could facilitate the ion diffusion during the electrochemical reactions. In addition, the presence of multiple peaks between 80 and 300 cm^{-1} corresponds to Raman modes of A_g and B_{3g}, which are typically observed in layered SnS structures.[30,31] The peaks observed at 93 and 199 cm^{-1} can be attributed to the wagging and breathing mode A_g vibrations, while the peak around 226 cm^{-1} is attributed to the "NaCl" type vibration in the SnS layered structures. A few other peaks observed at 164 and 202 cm^{-1} correspond to the B_{3g} vibration in the zigzag direction. Such observations indicate that the formed SnS structures maintain a layered structure, which could significantly improve charge storage capabilities and ion diffusion pathways.

Surface composition and chemical bonding of the nanostructures were further evaluated by XPS. The carbon (~284.8 eV) and oxygen (~531.5 eV) were visible in both structures, along with the peaks corresponding to Sn 3d (~486 eV) and S 2p (~161.5 eV) in SnS@VCN structures (Figure 3b). Compared with VCN structures, carbon signals are more attenuated in the hybrid structure, which could be due to the overgrown SnS features. Therefore, the high-resolution C 1s spectra were compared, and it was illustrated that the C 1s in SnS@VCN is broadened in both the lower- and higher binding-energy regions. This could be due to the possible interfacial interactions via C-S or C-Sn bonding, charge-transfer effects, or formation of structural defects, which are typically observed in the carbon-transition metal sulfide structures.

The C 1s spectrum of VCN is fitted to various components, including sp^2 C-C at 284.8 eV, sp^3 C-C at 285.5 eV, C-OH at 286.3 eV, C-O-C at 287.3 eV, C=O at 289.4 eV, a π-π* shake-up satellite at 291.4 eV, and a small component around 284.1 eV, which corresponds to vacancy defects.[4,28] High-resolution Sn 3d spectra of SnS@VCN appeared with two major components, Sn $3d_{5/2}$ (486.6 eV) and Sn $3d_{3/2}$ (495.1 eV), with each of them deconvoluted to two components: Sn^{2+} $3d_{5/2}$ at 485.5 eV, Sn^{4+} $3d_{5/2}$ at 486.6 eV, Sn^{2+} $3d_{3/2}$ at 493.9 eV, and Sn^{4+} $3d_{3/2}$ at 495.1 eV.[32,33] The corresponding S 2p spectra deconvoluted with two peaks, attributed to S $2p_{3/2}$ and S $2p_{1/2}$ peaks located at 161.7 and 162.8 eV, respectively, ascribed to S^{2-} species that could be attached to the Sn oxidation states. All the interpretations based on the physico-chemical characterizations suggest that plasma-assisted sulfurization enables rapid conversion of Sn to SnS, supported by the VCN backbone, forming a coaxial core–shell hybrid structure that ensures good adhesion, structural integrity, and a

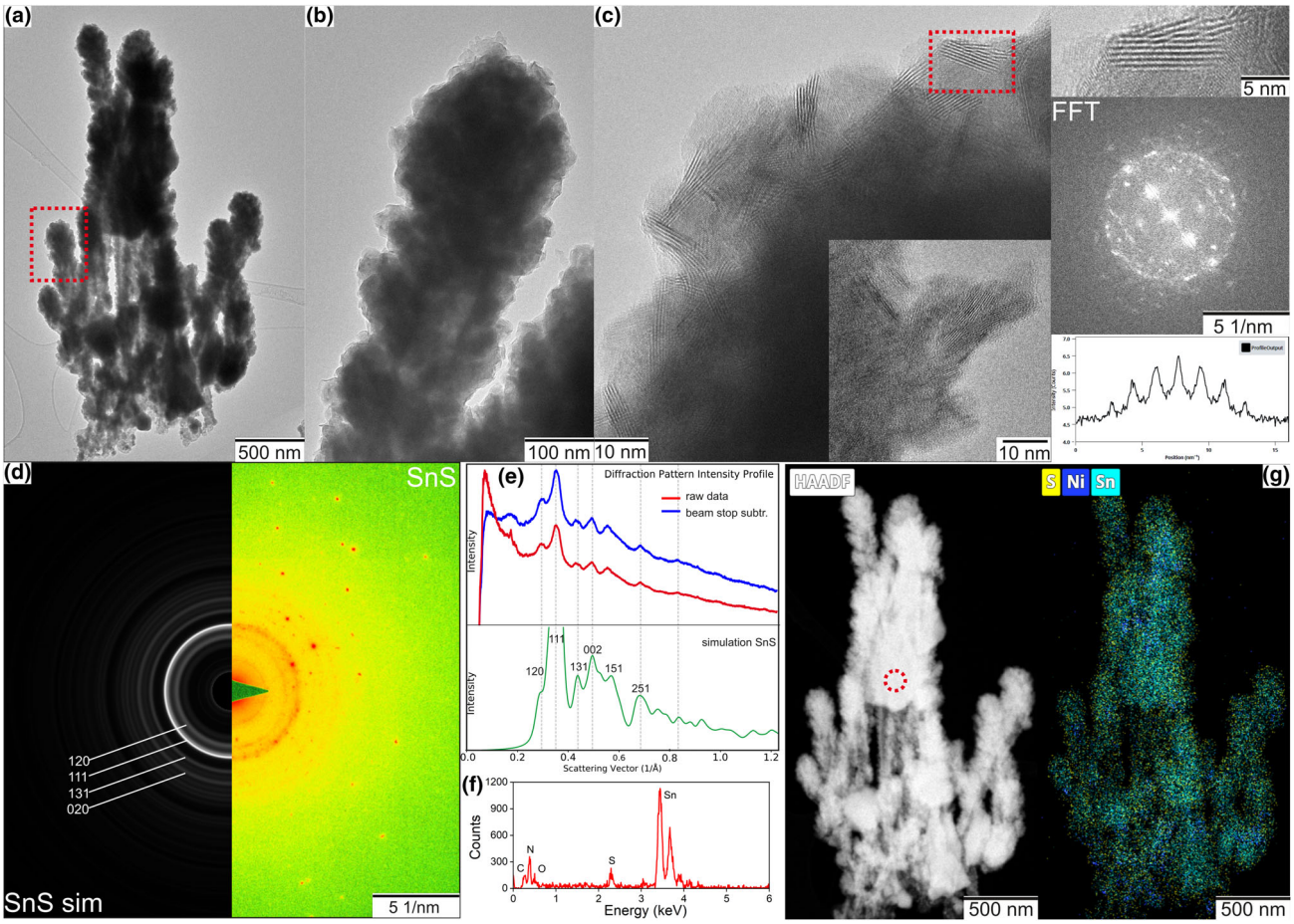

Figure 2. Microstructure of the SnS–VCN nanostructures: a) conventional TEM micrograph of SnS@VCN, with b) magnified region showing carbon NW core, overgrown by SnS. c) Surface details showing polycrystalline layered sheets of SnS (details in insets), with corresponding FFT and intensity profile graph. d) Simulated and experimental SAED patterns, indexed for orthorhombic SnS. e) Diffraction pattern intensity profile (red – raw, blue – beam stopper contribution subtracted) and simulated graph from reference SnS data, with marked crystal planes. f) Results of EDS point analysis showing S and Sn, with minimum O content (analysis point marked by red circle), and g) STEM-EDS spatial distribution mapping of principal components, visualized using S-Kα, Ni-Kα, and Sn-Lα energy lines.

hierarchical morphology with a large surface area for electrode–electrolyte interaction and rapid ion diffusion, making them promising electrode materials for SCs.

2.2. Electrochemical Characterization

The electrochemical behavior of plasma-designed binder-free electrodes was evaluated in a three-electrode setup, with CV, GCD, and impedance analysis. The binder-free approach ensures excellent interfacial contact, uniform dispersion of active species, and the removal of non-conductive polymeric binders, which are often responsible for impeding charge transport. All the plasma-designed electrodes: VCN, Sn@VCN, and SnS@VCN were compared to see the changes in performance due to the unique coaxial core–shell morphology. Initially, all electrodes were subjected to CV analysis over a potential window of 0–0.5 V at scan rates of 10–100 mV s^{-1}. A comparison of the CV in **Figure 4**a shows that the pristine VCN produced on Ni foam exhibits limited electrochemical activity. A significant increase in current density and a notable expansion of the enclosed CV area were observed after plasma-assisted anchoring of Sn (Sn@VCN), indicating improved charge storage capacity. The CV profiles showed distinct redox peaks, indicating the contribution of faradaic processes. The hybrid SnS@VCN electrode exhibited the highest current response, possibly due to its enhanced electrochemical reactivity. Strong electronic interaction between SnS nanostructures and the VCN scaffold, and altered charge-transfer kinetics, are suggested by the minor shifts in the anodic and cathodic peak potentials relative to pure VCN. The reversible redox reactions of SnS species inside the applied potential window could be the cause of the pseudocapacitive, battery-like behavior.[34,35] The CV profile of SnS@VCN at scan rates from 10 to 100 mV s^{-1} shows a progressive increase with scan rate, indicating a surface-controlled pseudocapacitive mechanism (Figure 4c; the corresponding figure for Sn@VCN is presented in Figure S2a, Supporting Information). It was also observed a slight shift in their redox peak potentials at high scan rates due to ion-diffusion constraints and charge-transfer resistance.

To understand the charge storage capacity of electrodes, galvanostatic charge–discharge (GCD) tests were performed at different current densities (3–12 A g^{-1}) for all the electrodes. The GCD curves (Figure 4b) show that the specific capacitance increases significantly with the gradual

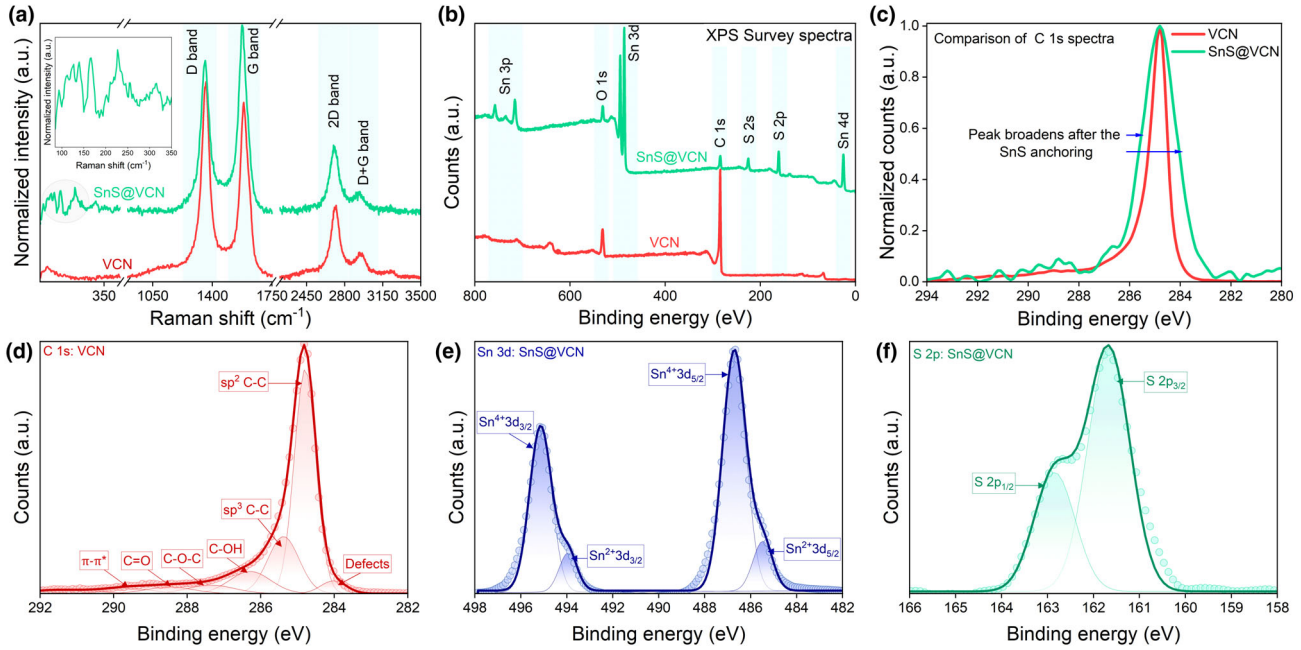

Figure 3. Structural and chemical analysis of the nanostructures. a) Raman spectra, b) XPS survey spectra, and c) comparison of the high-resolution C 1 s spectra of the VCN and SnS@VCN; d) deconvoluted C 1 s spectra of VCN; e) deconvoluted Sn 3d and f) S 2p spectra of SnS@VCN hybrid structures.

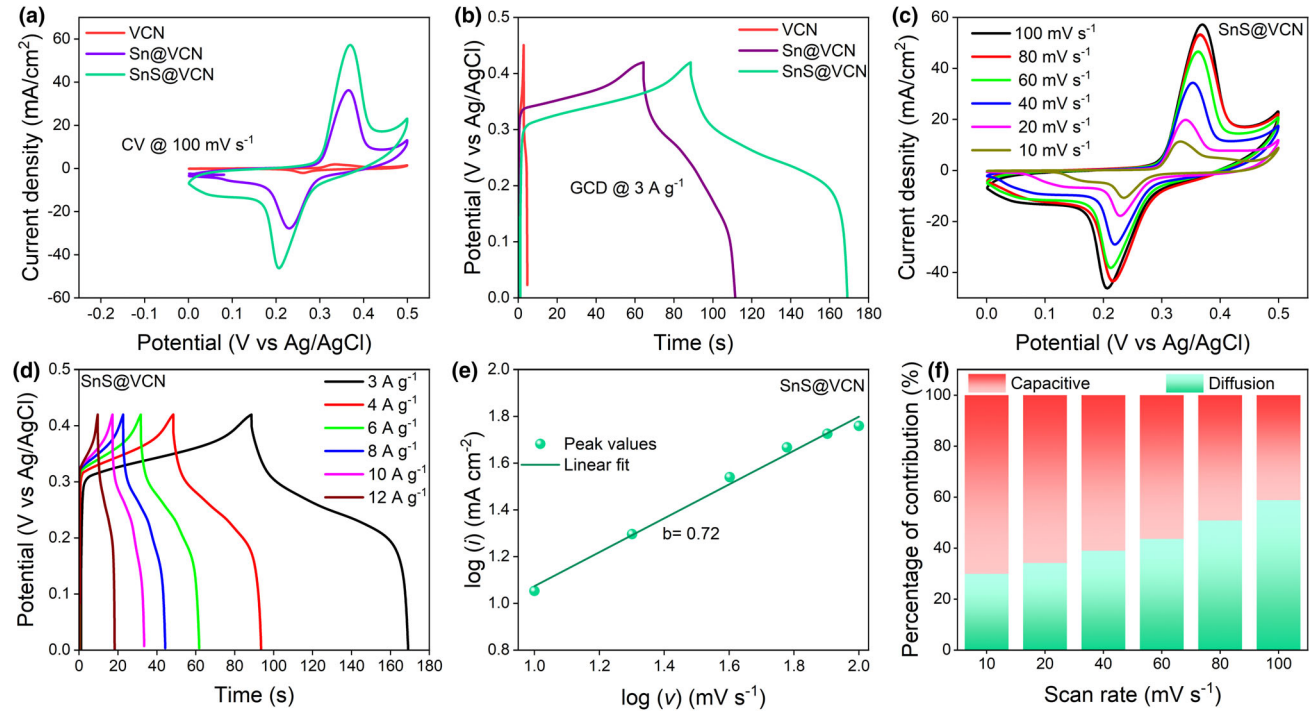

Figure 4. Electrochemical evaluation of the electrodes using a three-electrode configuration. a) CV comparison at a scan rate of 100 mV s^{-1} and b) GCD at 3 A g^{-1} of VCN, Sn@VCN, and SnS@VCN; c) CV at different scan rates and d) rate capability of SnS@VCN; e) log (i) versus log (v) graph and f) contribution from different electrochemical storage mechanisms of SnS@VCN.

addition of Sn, followed by sulfurization to prepare SnS@VCN. The VCN electrode displayed a linear-type discharge curve with a capacitance of 128 F g^{-1}, which can be ascribed to the electric double-layer capacitance. The GCD profiles gradually change into nonlinear, battery-type curves with discrete potential plateaus upon Sn incorporation and the subsequent addition of SnS, demonstrating dominating faradaic redox

processes. The specific capacitance of the prepared Sn@VCN and SnS@VCN at a current density of 3 A g^{-1} is 392 F g^{-1} (164 C g^{-1}) and 577 F g^{-1} (242 C g^{-1}), respectively. Considering that the SnS@VCN electrodes demonstrated the highest current response and charge storage performance, further electrochemical features were characterized to assess the electrode potential. The capacitance retention of the electrode at higher current densities was evaluated at multiple current densities and calculated to be 577 F g^{-1} (242 C g^{-1}) at 3 A g^{-1} and 414 F g^{-1} (174 C g^{-1}) at 12 A g^{-1} (Figure 4d, corresponding studies on Sn@VCN are presented in Figure S2b, Supporting Information). The rate capability comparison of electrodes indicates that the SnS@VCN electrode retained approximately 72% of its initial capacitance, whereas the Sn@VCN electrode maintained only 52% at a higher current density of 12 A g^{-1}. In addition, both electrodes maintained excellent coulombic efficiencies above 90%, with SnS@VCN achieving 99% at 12 A g^{-1} (Figure S3, Supporting Information). As the charge storage mechanism of SnS@VCN is primarily governed by reversible faradaic reactions of Sn-based species in alkaline electrolyte, which can be represented as:

$$Sn^{2+} + 2OH^- \rightleftharpoons Sn(OH)_2 \quad (1)$$

$$SnS + 2OH^- \rightleftharpoons Sn(OH)_2 + S^{2-} + 2e^- \quad (2)$$

These reversible surface redox reactions, coupled with the conductive electrostatically charging VCN backbone and binder-free architecture, result in enhanced capacitive behavior. Therefore, a quantitative analysis of the charge-storage mechanism in the SnS@VCN electrode was performed using Dunn's method, distinguishing between diffusion-controlled and capacitive contributions at different scan rates. The power-law equation describes the relationship between the measured current (i) and scan rate (v):

$$i = av^b \quad (3)$$

where a and b are adjustable parameters. The slope of the linear fit of the log(i) vs log(v) plot was used to get the b-value, estimated as 0.72, indicating a combined contribution of both surface-controlled and diffusion-limited processes (Figure 4e). To further understand the charge storage mechanism and evaluate the contribution quantities, the total current response at a fixed potential was determined by:

$$i(V) = K_1 v + K_2 v^{1/2} \quad (4)$$

where i corresponds to the current (A) at a specific potential, K_1 corresponds to the linear regression slope, and K_2 corresponds to the intercept of the $i_{(v)}/v^{1/2}$ vs $v^{1/2}$ (Figure S4, Supporting Information). At different scan rates, the relative contributions of capacitive and diffusion-type mechanisms were calculated and presented in Figure 4f. The analysis reveals that capacitive processes contribute around 29.9%, while diffusion-controlled processes dominate at 70% at lower scan rates, with the contribution increasing progressively at higher scan rates due to enhanced surface redox properties. This behavior confirms that the SnS@VCN electrode exhibits a synergistic charge storage mechanism arising from the combined contributions of surface-controlled and diffusion-controlled processes. The VCN network enhances electrical conductivity and mainly contributes to electric double-layer capacitance, while the SnS component provides pseudocapacitive behavior with an additional diffusion-controlled contribution, leading to the observed mixed kinetics.

In addition to charge storage, the remarkable electrochemical stability of the SnS@VCN electrode is a crucial characteristic that ensures reliable operation in cutting-edge supercapacitor devices. To ensure long-term durability and economic viability in energy storage applications, supercapacitors must withstand thousands of charge–discharge cycles without significant loss of capacitance. Therefore, continuous GCD measurements were used to assess the coulombic efficiency and long-term cycling performance of SnS@VCN at a high current density of 12 A g^{-1}, as presented in **Figure 5**a. After 10 000 cycles of stability testing, the electrode demonstrated exceptional capacitance retention of 115% and nearly 100% coulombic efficiency. It was observed that stability decreased slightly in the first few cycles, followed by a gradual increase, which may be due to electrochemical activation of the electrode surface and progressive electrolyte infiltration into previously inaccessible active areas. To assess electrode behavior and charge transfer during electrochemical stability testing, the impedance characteristics of the material were evaluated before and after the stability test. The EIS analysis reveals that the electrode solution resistance remains nearly unchanged before and after the stability studies, at approximately 0.95 and 1.0 Ω, respectively (Figure 5b), indicating stable electrolyte conductivity and preserved electrode integrity. It was also observed that the charge-transfer resistance (R_{ct}) did not increase with extended cycling, from ~0.6 Ω before cycling to 0.4–0.5 Ω after stability, which could lead to the enhanced 115% retention and points to electrochemical activation rather than deterioration. Following stability testing, the R_{ct} remained constant or slightly decreased, indicating enhanced interfacial electron transfer kinetics, which can be attributed to surface remodeling or enhanced electrolyte accessibility.[36] The Bode plots further clarify the interfacial dynamics, which exhibit a broad phase angle maximum at intermediate frequencies before stability, indicative of capacitive charge accumulation and faradaic processes (Figure S5, Supporting Information). The phase angle distribution changes and becomes more frequency-dispersed after stabilization, signifying changes in the surface heterogeneity and interfacial capacitance. A decrease in pure capacitive dominance and an increase in faradaic contribution are suggested by a decrease in the maximum phase angle at intermediate frequencies.[37,38] Finally, no inductive loop or phase inversion is seen, indicating the electrode's structural soundness even under extended use. The capacitance retention suggests progressive electrode activation during long-term cycling. This behavior can be attributed to gradual electrolyte penetration into the porous structure, improved wettability of the electrode surface, and enhanced accessibility of initially less-utilized redox-active sites.[39,40] The EIS results collected at different cycles show a reduction in interfacial/charge-transfer resistance, supporting improved reaction kinetics during cycling (Figure S6, Supporting Information). The reduced intercept at the high-frequency region and the steeper slope in the low-frequency region indicate a decrease in internal/charge-transfer resistance and an improvement in ion diffusion behavior. This change suggests that repeated cycling promotes better electrolyte penetration into the electrode structure and enhances the accessibility of electroactive sites. Meanwhile, the high coulombic efficiency indicates that the charge-storage process remains highly reversible, suggesting that the capacitance increase is mainly related to electrode activation rather than irreversible side reactions. All the electrochemical studies ensure that the fabricated SnS@VCN electrode exhibits one of the best rate capability stabilities among the variously reported SnS-based electrodes, as shown in Figure 5c and Table S1,

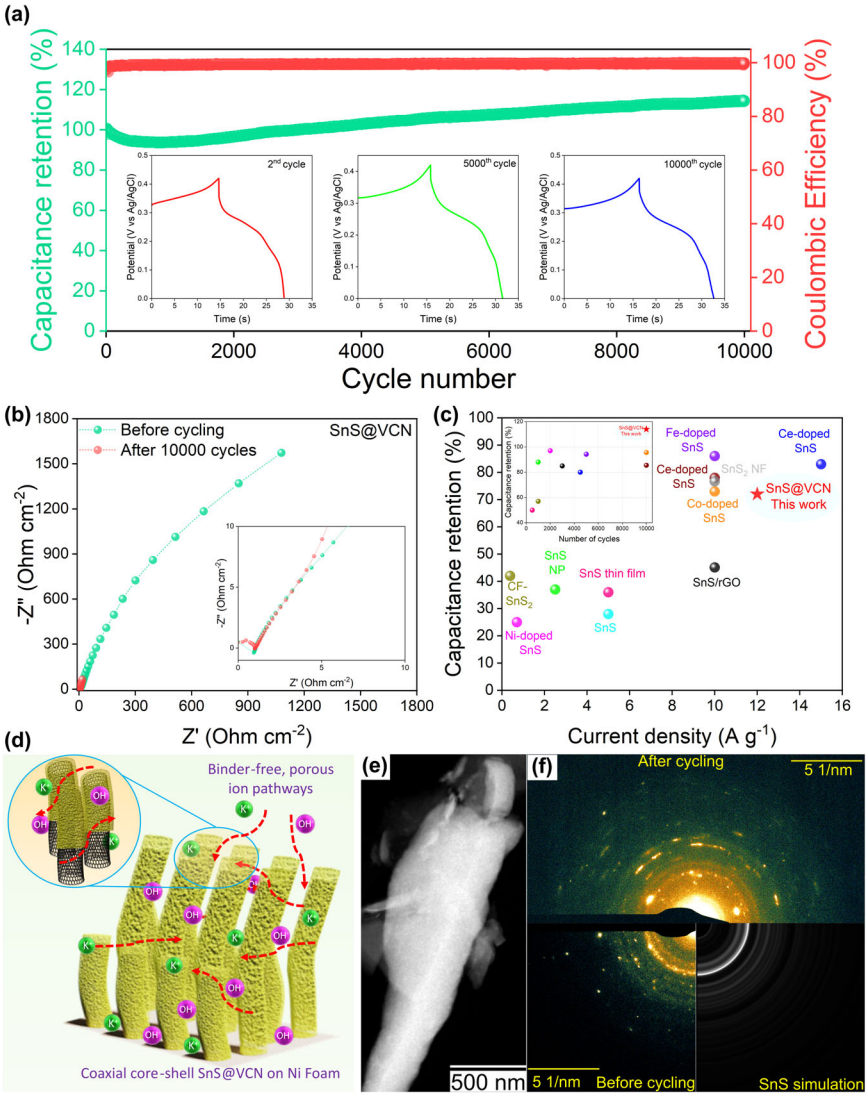

Figure 5. a) long-term stability studies of SnS@VCN electrodes cycled for 10 000 cycles at a current density of 12 A g^{-1}; b) EIS studies of the electrode before and after stability testing; c) comparison of rate capability performance of the SnS@VCN electrode materials to the state-of-the-art peer materials, along with the comparison of cyclic performance inset. d) A possible charge storage pathway in SnS@VCN electrodes. Post-mortem analysis of the electrode material after the stability testing. e) HAADF-STEM micrograph showing homogenous distribution of principal elements (uniform contrast), and f) experimental SAED patterns: simulated pure SnS, before, and after the cycling testing, with reference SnS simulated pattern. The morphology of the individual SnS@VCN is preserved, and no detrimental changes in the crystal structure were observed.

Supporting Information.[14,41–53] The enhanced charge storage and ultra-stable performance of SnS@VCN can be ascribed to the synergistic interaction between uniformly overgrown SnS and VCN within the well-defined coaxial core–shell architecture. By buffering the volume change of SnS during repeated redox reactions, the mechanically strong and highly conductive VCN backbone prevents structural pulverization and particle agglomeration.[54,55] The binder-free electrode design, achieved by direct growth of SnS@VCN on the conductive substrate, ensures close interfacial contact and continuous electron transport, unlike traditional slurry-coated electrodes with polymeric binders such as PVDF, which can block active sites and raise internal resistance.[56,57]

The direct contact between the current collector and the active material minimizes diffusion pathways, and, as a highly conductive backbone, the VCN core provides continuous electron transport channels, lowering internal resistance and accelerating charge transfer. In addition, the hierarchical morphology allows rapid electrolyte penetration and enhanced faradaic reaction kinetics owing to the nanoscale thickness of the shell, which drastically reduces ion diffusion paths, particularly at higher current densities, resulting in high-rate performance. Based on these advantages of the plasma-designed SnS@VCN electrodes, a possible charge-diffusion pathway is shown in Figure 5d.

Considering the electrochemical stability of the electrode is also associated with the structural integrity of the active material, the ensured structural stability of SnS@VCN after harsh cycling conditions was analyzed by *ex situ* TEM of electrodes after 10 000 cycles (Figure 5e). The uniform chemical composition, even after the harsh electrochemical testing, is confirmed by STEM-EDS mapping of the spatial distribution of principal components, Sn and S (Figures S7 and S8, Supporting Information). The crystal structures of the electrode materials after cyclic stability, as determined from the SAED patterns, were compared with those of pristine SnS@VCN electrodes and the simulated SnS pattern, showing no detrimental changes (Figure 5f, Figures S7 and S8, Supporting Information). In addition, the EDS spectra of the cycled electrodes obtained from the SEM demonstrate a significant presence of potassium and oxygen, while the presence of sulfur and Sn is diminished, indicating the excellent electrode–electrolyte interaction (Figure S9, Supporting Information).

2.3. Fabrication of SnS@VCN//AC Asymmetric Supercapacitors

To assess the real-time applicability of the SnS@VCN electrodes, an aqueous asymmetric full cell was fabricated utilizing SnS@VCN as the positive electrode and activated carbon (AC) as the negative electrode. The corresponding CV curves and GCD of activated carbon are presented in Figure S10, Supporting Information. The SnS@VCN//AC device was fabricated using the mass-balance method, and CV curves at varying scan rates over a potential range of 0–1.6 V are presented in **Figure 6**a. The CV profiles displayed both quasi-rectangular and distinct redox peaks, confirming a hybrid storage mechanism where the EDLC behavior arises from the AC and a mixed capacitance performance from SnS@VCN electrodes. Fast charge propagation and good rate capability are indicated by the current response increasing proportionately without a change in curve shape as the scan rate increases from 10 to

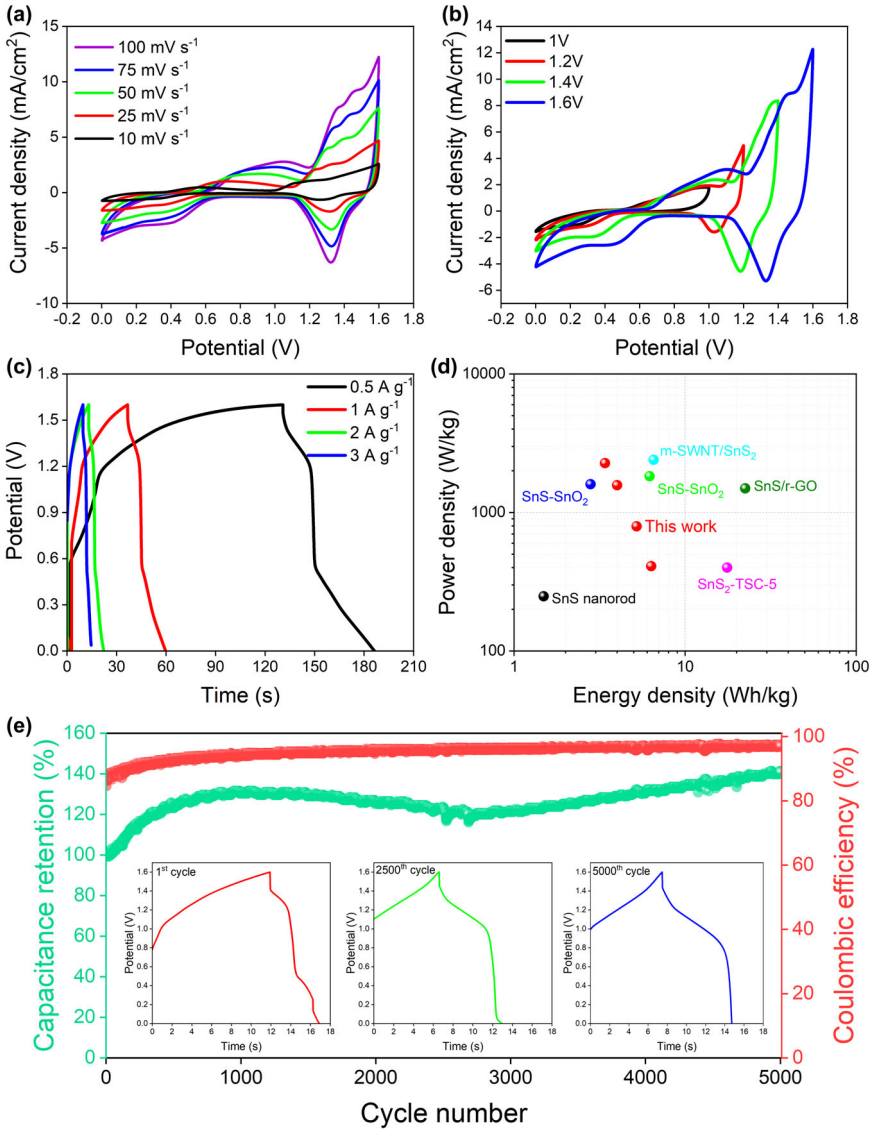

Figure 6. Electrochemical performance of the fabricated SnS@VCN//AC full cell. a) CV at different scan rates; b) at different voltages; c) GCD at different current densities; d) Ragone plot comparison of the fabricated device with other SnS-based supercapacitors; e) long-term stability of the fabricated full cell for 5000 cycles.

100 mV s^{-1}. The overall reversibility remains substantial, indicating steady kinetics and excellent conductivity enabled by the conductive VCN scaffold. It is observed that the enclosed CV area increases significantly when the operating window is enlarged from 1.0 to 1.6 V, allowing the device to retain more charge at higher voltages (Figure 6b). The charge–discharge curves display a quasi-triangular profile with minor deviations from linearity, reflecting the coexistence of both EDLC behavior from the VCN and pseudocapacitive/faradaic contributions from SnS (Figure 6c). The calculated specific capacitance values for the SnS@VCN//AC device were 17.8, 14.6, 11.2, and 9.6 F g^{-1} at current densities from 0.5 to 3 A g^{-1}. As anticipated, the discharge time decreases with increasing current density; however, the curves maintain their optimal shape, suggesting strong reversibility and structural integrity under rapid cycling. Low internal resistance is implied by the modest IR drop, consistent with the binder-free VCN design, which provides strong electrical contact and rapid electron transport. The ASC fabricated in this work provided a competitive balance of energy and power density of 6.32 Wh kg^{-1} and 410 W kg^{-1}, respectively, which positions them as comparable to similar materials as presented in the Ragone plot (Figure 6d).

Apart from energy performance, durability is a key parameter; thus, the cycling stability of the SnS@VCN//AC device is shown in Figure 6e, where the stability curve clearly indicates electrochemical activation rather than deterioration, with a rise in capacitance retention to ≈140%. The porous coaxial core–shell networks in SnS@VCN enhance cycle life by promoting greater ion accessibility and active surface exposure. Additionally, during extended cycling, the coulombic efficiency remains close to 100%, indicating that the device exhibits a highly reversible charge-storage mechanism. The 1st, 2500th, and 5000th cycle GCD curves (Figure 6e inset) with excellent reversibility confirm the outstanding mechanical and electrochemical integrity of the binder-free electrode throughout extended use, maintaining a consistent shape.

Inorder to confirm the reproducibility and robustness of the electrode, the stability performance was repeated on an additional full cell, and the initial GCD curves were examined (Figure S11, Supporting Information). The full cell shows a similar increase in capacitance and enhanced stability after 5000 cycles, which can be attributed to gradual electrode activation and improved accessibility of redox-active sites, facilitated by enhanced electrolyte penetration into previously less accessible regions. The GCD curves at early stages (1st, 10th, 50th, 100th, and 1000th cycles) show a slight decrease during the initial cycles (10th–50th), then gradually increase from 100 to 1000 cycles. This behavior suggests that an initial stabilization process occurs, followed by electrode activation, leading to enhanced capacitance. Besides, the highly conductive VCN backbone, along with the presence of voids and structural defects observed between SnS@VCN structures, could also facilitate ion transport and buffer volume changes, thereby enhancing electrochemical stability and enabling the potential of the material for long-standing applications.

3. Conclusion

In this work, a metal sulfide–carbon nanostructure-based coaxial core–shell hybrid electrode was fabricated for high-performance supercapacitor applications. A rapid plasma-assisted, soft-chemistry, dry approach was used to synthesize vertical nanocarbon (VCN) uniformly

overgrown with a SnS layered structure. The designed SnS@VCN electrode demonstrated battery-type charge-storage performance for supercapacitors, delivering a capacitance of 577 F g^{-1} (242 C g^{-1}) at a current density of 3 A g^{-1} and an excellent rate capability of 72% at 12 A g^{-1}, placing it among the best-performing SnS-based electrodes reported to date. Remarkably, the electrode demonstrates exceptional electrochemical stability, with capacitance retention of ∼115% after 10 000 cycles, indicating progressive activation and outstanding structural robustness. These outstanding performances stem from the unique coaxial core–shell morphology of the electrode, which provides abundant electroactive sites and efficient charge transport pathways. An asymmetric device fabricated using the SnS@VCN//AC delivered a capacitance of 17.8 F g^{-1} at 0.5 A g^{-1}, with competitive energy and power densities of 6.32 Wh Kg^{-1} and 410 W kg^{-1}, respectively. Notably, the device maintains 140% capacitance retention with nearly 100% coulombic efficiency, underscoring its superior long-term durability. The electrode fabrication technique demonstrated in this work is one of the fastest methods (<2 h) and ensures minimal chemical residues owing to its plasma-assisted, dry processing. The excellent rate capability and ultrahigh stability of SnS@VCN represent a substantial advancement over conventional SnS-based battery-type electrodes, which typically exhibit low-rate capability and stability. In this regard, this work addresses a critical challenge in battery-type electrodes and opens a pathway for designing ultra-durable high-rate supercapacitors for next-generation energy-storage devices.

4. Experimental Section

Synthesis of vertical nanocarbon structures (VCN): Vertical nanocarbon structures (VCN) were directly deposited on a 1.5 × 1.5 cm^2, 300 µm-thick nickel foam (purchased from Xiamen Zopin New Material Limited, China) using a low-pressure radiofrequency PECVD system. VCN structures were synthesized using the previously reported low-pressure plasma discharge protocols.[28,58] In brief, the plasma system used for VCN synthesis consists of a cross-type glass tube with an 8 cm diameter, and each arm is 40 cm long. A Nagoya type-III coil was used to inductively couple the system to a radiofrequency generator, which was externally air-cooled. The nickel substrate was placed into the plasma discharge region using a grounded stainless steel substrate holder. Later, the system was pumped down to 2–4 Pa before the experiments, and methane was fed into the reactor with a maintained total pressure of 20 Pa. Lastly, the plasma was ignited at 800 W, and carbon deposition was maintained continuously for 10 min. The substrate holder was not externally heated; however, the temperature during the growth process was monitored at 750–800 °C due to plasma heating.

Synthesis of hierarchical SnS@VCN hybrid nanostructure: The VCN, directly grown on nickel foam, served as a conductive matrix for the design of a hybrid nanoarchitecture with SnS. As the first step, a thin Sn layer was deposited by magnetron sputtering at low pressure for 10 min to achieve a uniform thickness of 100 nm. Later, the as-obtained VCN/Sn was converted to SnS@VCN via a rapid plasma conversion process using H_2S as the reactive gas. The plasma conversion process was conducted in a low-pressure radiofrequency (RF) plasma system consisting of an 80 cm-long glass tube with a 4 cm diameter.[59] An internally water-cooled inductive coil was used to couple the RF generator to the plasma chamber. The VCN/Sn samples were placed in the post-glow region of the chamber, 10 cm downstream from the plasma discharge region. The plasma chamber was pumped down to 2 Pa prior to the experiments, and the reactive gas H_2S (Ar + 2% H_2S) was fed into the system at a flow rate of 100 sccm. The total pressure during the treatment was 25 Pa, the plasma was ignited at 200 W, and the treatment lasted 5 min. This low-power plasma approach ensures a low surface temperature and prevents any detrimental alterations to the hierarchical morphology.

Material characterization: Surface and structural analysis—Various surface and structural analysis techniques were used to characterize the final hybrid SnS@VCN nanostructures. Surface morphology of the plasma-designed VCN and SnS@VCN hybrid nanostructure was examined by scanning electron microscope (SEM, Verios 4G HP, Thermo Fisher Scientific) equipped with an energy-dispersive X-ray spectrometer (EDS, UltimMax SDD, Oxford Instruments).

The chemical and phase composition of the nanostructures was assessed by a transmission electron microscope (S/TEM, Talos 200X G2, Thermo Fisher Scientific). The samples were sonicated in ethanol (abs) to release the nanostructures from the nickel foam substrate, and the dispersion was drop-casted onto commercial Cu-supported amorphous carbon grids for the TEM analysis.

The changes in the structural quality of the VCN and SnS@VCN and in their chemical fingerprints were analyzed using Raman spectroscopy (NT-MDT SI, Moscow, Russia). The spectra were recorded at multiple points on the samples using a laser with an excitation wavelength of 488 nm.

The surface chemistry and chemical composition of the samples were examined by X-ray photoelectron spectroscopy on a Genesis XPS spectrometer from ULVAC-PHI, equipped with an Al monochromatic source. The analyzed area was 0.1 mm in diameter. A low-energy electron flood gun and a low-energy Ar-ion beam were used during measurements to reduce charging.

Electrochemical characterizations—The plasma-designed VCN-based hybrid nanostructures, directly deposited on nickel foam, were used as a binder-free electrode material for electrochemical studies without using any conductive carbon or polymeric binders. To compare the effect of different components in the hybrid electrode, VCN, Sn@VCN, and SnS@VCN were used as the active electrodes. The initial electrochemical performance was assessed using a conventional three-electrode setup, with the plasma-designed electrodes as the working electrodes, Ag/AgCl as the reference electrode, and a platinum wire as the counter electrode. The three-electrode measurements were conducted in 3 M KOH, and cyclic voltammetry (CV) was acquired at different scan rates (10–100 mV s^{-1}) within a potential window from 0 to 0.45 V (vs Ag/AgCl); the galvanostatic charge–discharge (GCD) was conducted at different current densities (1–12 A g^{-1}); impedance features of electrodes were analyzed by electrochemical impedance spectroscopy (EIS), and the measurements were performed between the frequency ranges of 0.01 Hz–100 kHz by applying an open circuit potential with an AC amplitude of 5 mV.

An asymmetric two-electrode Swagelok device was fabricated using SnS@VCN as the positive electrode and activated carbon (AC) as the negative electrode, with 3 M KOH as the electrolyte. A 10 mm disc was cut from the SnS@VCN binder-free electrode and used directly as a positive electrode without any further treatment. Similarly, a 10 mm disc of AC electrode was used as the negative electrode, prepared by slurry coating of AC and conductive carbon black with a polyvinylidene fluoride (PVDF) binder. All electrochemical reactions, including CV, GCD, and stability tests, were conducted on a multichannel potentiostat (Model CS310X).

Acknowledgements

This research is supported by the Slovenian Research Agency (ARIS) research program P1-0417, research grant J2-50074; EU Graphene Flagship FLAG-ERA III JTC 2021 project "VEGA" (2021–05924, MIZS-PR-11938) and M-ERA. NET 3 project ANGSTROM (Project ANGSTROM was selected in the Joint Transnational Call 2023 of M-ERA.NET 3, which is an EU-funded network of about 49 funding organizations - Horizon 2020 grant agreement No 958174 and the project is funded by Ministrstvo za visoko šolstvo, znanost in inovacije – MVZI, Slovenia (PR-13503)). The authors acknowledge the support from Prof. Miha Čekada for the plasma-enabled sputtering experiments.

Conflict of Interest

The authors declare no conflict of interest.

Supporting Information

Supporting Information is available from the Wiley Online Library or from the author.

Keywords

coaxial core–shell, cyclic stability, supercapacitors, tin sulfide, vertical nanocarbon

Received: March 4, 2026
Revised: April 14, 2026
Published online: April 15, 2026

[1] Q. Dou, H. S. Park, *Energy Environ. Mater.* **2020**, *3*, 286.
[2] Q. Zhu, D. Zhao, M. Cheng, J. Zhou, K. A. Owusu, L. Mai, Y. Yu, *Adv. Energy Mater.* **2019**, *9*, 1901081.
[3] L. Kong, M. Liu, J. Cao, R. Wang, W. Zhang, K. Yan, X. Li, F. C. Walsh, *Advances in Energy Storage*, John Wiley & Sons, Ltd, Hoboken, NJ **2022**, pp. 71–98.
[4] N. M. Santhosh, K. K. Upadhyay, P. Stražar, G. Filipič, J. Zavašnik, A. Mão de Ferro, R. P. Silva, E. Tatarova, M. F. Montemor, U. Cvelbar, *ACS Appl. Mater. Interfaces* **2021**, *13*, 20559.
[5] A. Stott, M. O. Tas, E. Y. Matsubara, M. G. Masteghin, J. M. Rosolen, R. A. Sporea, S. R. P. Silva, *Energy Environ. Mater.* **2020**, *3*, 389.
[6] J. Liu, C. Wu, I. D. Gates, B. Jia, Z. Huang, T. Ma, *Energy Environ. Mater.* **2023**, *6*, e12520.
[7] H. Li, F. Qi, F. Yang, Z. Sun, *J. Colloid Interface Sci.* **2021**, *587*, 302.
[8] F. Qi, L. Shao, X. Shi, F. Wu, H. Huang, Z. Sun, A. Trukhanov, *J. Colloid Interface Sci.* **2021**, *601*, 669.
[9] J. Theerthagiri, K. Karuppasamy, G. Durai, A. U. H. S. Rana, P. Arunachalam, K. Sangeetha, P. Kuppusami, H.-S. Kim, *Nano* **2018**, *8*, 256.
[10] E. S. Sowbakkiyavathi, S. P. Arunachala Kumar, D. K. Maurya, B. Balakrishnan, J. Z. Guo, A. Subramania, *Adv. Compos. Hybrid Mater.* **2024**, *7*, 130.
[11] M. Setayeshmehr, M. Haghighi, K. Mirabbaszadeh, *Energy Storage* **2022**, *4*, e295.
[12] D. Mishra, N. Kumar, T. M. Patil, T. Na, S. H. Jin, *J. Alloys Compd.* **2025**, *1010*, 177582.
[13] R. Kumar Mishra, G. Jin Choi, R. Verma, S. Hun Jin, R. Bhardwaj, S. Arya, J. Singh, J. Seog Gwag, *Mater. Sci. Eng. B* **2024**, *303*, 117292.
[14] C. D. Jadhav, G. P. Patil, M. Amar, S. Lyssenko, R. Minnes, *J. Power Sources* **2024**, *623*, 235496.
[15] H. Chauhan, M. K. Singh, S. A. Hashmi, S. Deka, *RSC Adv.* **2015**, *5*, 17228.
[16] D. Chatterjee, S. Das, *RSC Sustain.* **2025**, *3*, 450.
[17] P. Sakthi, J. Uma, B. Balraj, K. Arulvendhan, *Sci. Rep.* **2025**, *15*, 22747.
[18] L. Rani, J. I. Han, *J. Energy Storage* **2023**, *74*, 109403.
[19] N. M. Santhosh, G. Filipič, E. Tatarova, O. Baranov, H. Kondo, M. Sekine, M. Hori, K. Ostrikov, U. Cvelbar, *Micromachines* **2018**, *9*, 565.
[20] M. Meyyappan, *J. Phys. D. Appl. Phys.* **2009**, *42*, 213001.
[21] S. Hussain, E. Kovacevic, J. Berndt, N. M. Santhosh, C. Pattyn, A. Dias, T. Strunskus, M.-R. Ammar, A. Jagodar, M. Gaillard, C. Boulmer-Leborgne, U. Cvelbar, *Nanotechnology* **2020**, *31*, 395604.
[22] Z. Bo, Y. Yang, J. Chen, K. Yu, J. Yan, K. Cen, *Nanoscale* **2013**, *5*, 5180.
[23] M. Tanemura, K. Iwata, K. Takahashi, Y. Fujimoto, F. Okuyama, H. Sugie, V. Filip, *J. Appl. Phys.* **2001**, *90*, 1529.
[24] M. S. Bell, K. B. K. K. Teo, R. G. Lacerda, W. I. Milne, D. B. Hash, M. Meyyappan, *Pure Appl. Chem.* **2006**, *78*, 1117.
[25] M. Kumar, *Nanotechnol. Percept.* **2010**, *6*, 7.
[26] Z. Wang, J. Chen, S. Sun, Z. Huang, X. Zhang, X. Li, H. Dong, *Energy Storage Mater.* **2022**, *50*, 161.
[27] N. M. Santhosh, K. K. Upadhyay, G. Filipič, J. Zavašnik, M. de Fátima Montemor, U. Cvelbar, *Carbon* **2023**, *203*, 686.
[28] N. M. Santhosh, V. Shvalya, M. Modic, N. Hojnik, J. Zavašnik, J. Olenik, M. Košiček, G. Filipič, I. Abdulhalim, U. Cvelbar, *Small* **2021**, *17*, 2103677.
[29] A. Gohier, C. P. Ewels, T. M. Minea, M. A. Djouadi, *Carbon* **2008**, *46*, 1331.
[30] S. Sohila, M. Rajalakshmi, C. Ghosh, A. K. Arora, C. Muthamizhchelvan, *J. Alloys Compd.* **2011**, *509*, 5843.
[31] M. Li, Y. Wu, T. Li, Y. Chen, H. Ding, Y. Lin, N. Pan, X. Wang, *RSC Adv.* **2017**, *7*, 48759.
[32] R. K. Yadav, P. S. Pawar, Y. T. Kim, I. Sharma, J. Heo, *J. Mater. Chem. A* **2024**, *12*, 3265.
[33] M. Choi, W. William, J. Hwang, D. Yoon, J. Kim, *J. Ind. Eng. Chem.* **2018**, *59*, 160.
[34] Y. Yang, S. Ren, X. Song, Y. Guo, D. Si, H. Jing, S. Ma, C. Hao, M. Ji, *Electrochim. Acta* **2016**, *209*, 350.
[35] W. He, K. Chen, R. Pathak, M. Hummel, K. M. Reza, N. Ghimire, J. Pokharel, S. Lu, Z. Gu, Q. Qiao, Y. Zhou, *Chem. Eng. J.* **2021**, *414*, 128638.
[36] S. Ahmad, T. U. Haq, A. Alam, M. Z. U. Shah, J. Feng, M. M. Alanazi, T. Saidani, *J. Alloys Compd.* **2025**, *1018*, 179196.
[37] J. Huang, Z. Li, B. Y. Liaw, J. Zhang, *J. Power Sources* **2016**, *309*, 82.
[38] K. Ashok Kumar, A. Pandurangan, S. Arumugam, M. Sathiskumar, *Sci. Rep.* **2019**, *9*, 1228.
[39] M. Z. Ansari, N. Parveen, D. K. Nandi, R. Ramesh, S. A. Ansari, T. Cheon, S.-H. Kim, *Sci. Rep.* **2019**, *9*, 10225.
[40] L. G. Ghanem, D. M. Sayed, N. Ahmed, M. Ramadan, N. K. Allam, *Langmuir* **2021**, *37*, 5161.
[41] E. Bao, J. Sun, Y. Liu, X. Ren, X. Liu, C. Xu, H. Chen, *Int. J. Hydrog. Energy* **2022**, *47*, 39204.
[42] I. Sarasamreen, S. Arun kumar, S. Shanavas, R. Ramesh, P. M. Anbarasan, A. Arunkumar, M. Shkir, P. Sivakumar, *Surf. Interfaces* **2024**, *54*, 105215.
[43] B. P. Reddy, M. C. Sekhar, S. V. P. Vattikuti, Y. Suh, S.-H. Park, *Mater. Res. Bull.* **2018**, *103*, 13.
[44] R. Barik, N. Devi, V. K. Perla, S. K. Ghosh, K. Mallick, *Appl. Surf. Sci.* **2019**, *472*, 112.
[45] Y. Li, H. Xie, J. Tu, *Mater. Lett.* **2009**, *63*, 1785.
[46] Y. Li, H. Xie, J. Wang, *J. Solid State Electrochem.* **2011**, *15*, 1115.
[47] B. Jansi Rani, S. Keerthana, G. Ravi, R. Yuvakkumar, D. Velauthapillai, M. Thambidurai, C. Dang, *Mater. Lett.* **2020**, *273*, 127958.
[48] M. Arif Dar, M. Y. Bhat, N. Ahmad Mala, H. Ahmad Rather, S. Venkatachalam, N. Srinivasan, *Mater. Today Proc.* **2022**, *66*, 1689.
[49] M. A. Dar, S. Dinagaran, K. M. Batoo, S. R. Ahamed, S. Hussain, Z. Ahmad, J.-J. Shim, *J. Energy Storage* **2023**, *68*, 107717.
[50] M. A. Dar, D. Govindarajan, K. M. Batoo, C. Siva, *J. Energy Storage* **2022**, *52*, 105034.
[51] R. K. Mishra, G. W. Baek, K. Kim, H.-I. Kwon, S. H. Jin, *Appl. Surf. Sci.* **2017**, *425*, 923.
[52] H. Wang, Y. Deng, W. Zhang, S. Yao, *J. Alloys Compd.* **2024**, *976*, 173402.
[53] J. Zou, S. Zhang, Y. Huang, J. Wang, X. Liu, S. Zhang, Y. Gao, C. Chen, M. Yu, *J. Alloys Compd.* **2023**, *965*, 171400.
[54] N. Venkatesh, S. Sivaramakrishnan, G. P. Nagaiah, G. Murugadoss, *Sci. Rep.* **2025**, *15*, 42324.
[55] D. Murugan, J. Arockiyasamy, G. Murugadoss, S. Sivaramalakshmi, N. Kumaresan, S. Ramesh, A. Pugazhendhi, *Ceram. Int.* **2025**, DOI: 10.1016/j.ceramint.2025.09.329.
[56] M. Isacfranklin, Y. Rathinam, R. Ganesan, D. Velauthapillai, *ACS Omega* **2023**, *8*, 11700.
[57] E. S. Agudosi, E. C. Abdullah, A. Numan, N. M. Mubarak, S. R. Aid, R. Benages-Vilau, P. Gómez-Romero, M. Khalid, N. Omar, *Sci. Rep.* **2020**, *10*, 11214.
[58] N. M. Santhosh, N. Shaji, P. Stražar, G. Filipič, J. Zavašnik, C. W. Ho, M. Nanthagopal, C. W. Lee, U. Cvelbar, *J. Energy Chem.* **2022**, *67*, 8.
[59] A. Baby, L. Martinčič, J. Zavašnik, A. Zidanšek, N. M. Santhosh, U. Cvelbar, *Chem. Eng. J.* **2025**, *525*, 170415.